International Journal of Fatigue 162 (2022) 106947

Contents lists available at ScienceDirect

International Journal of Fatigue

journal homepage: www.elsevier.com/locate/ijfatigue

Notch fatigue analysis and life assessment using an energy field intensity approach in 7050-T6 aluminium alloy under bending-torsion loading

R. Branco [a,*], J.D. Costa [a], L.P. Borrego [b,a], W. Macek [c], F. Berto [d]

[a] CEMMPRE, Department of Mechanical Engineering, University of Coimbra, Rua Luís Reis Santos, Coimbra, 3030-788 Coimbra, Portugal
[b] Department of Mechanical Engineering, Coimbra Polytechnic - ISEC, Rua Pedro Nunes, Quinta da Nora, 3030-199 Coimbra, Portugal
[c] Faculty of Mechanical Engineering and Ship Technology, Gdańsk University of Technology, 11/12 Gabriela Narutowicza Street, 80-233 Gdańsk, Poland
[d] Department of Mechanical and Industrial Engineering, NTNU, 7491 Trondheim, Norway

ARTICLE INFO

Keywords:
Energy field intensity
Fatigue life prediction
Crack initiation sites
Crack growth direction
Bending-torsion loading

ABSTRACT

This paper studies the fatigue crack initiation and fatigue crack propagation of notched cylindrical bars made of 7050-T6 aluminium alloy subjected to multiaxial bending-torsion loading. The sites of crack initiation and the angles of crack initiation were successfully predicted from the distribution of the first principal stress at the notch surface. Fatigue crack initiation lives were computed through the new concept of energy field intensity formalised in a linear-elastic framework along with a local stress-strain model for notch plasticity analysis. Regardless of the model used to compute the cyclic response at the geometric discontinuity, fatigue life predictions were in good agreement with the experimental observations.

1. Introduction

Aluminium alloys have a major application in aviation, aerospace, and automotive industries due to their low density, high strength, good fracture toughness, and attractive cost [1–2]. In these areas, a considerable number of critical components are exposed to cyclic multiaxial loading which makes them prone to fatigue failure [3–4]. Although the fatigue design often assumes that the materials are loaded in the elastic range, at the geometric discontinuities, plastic deformation can occur during the service period [5–6]. Thus, the development of accurate residual fatigue life predictions models based on damage tolerance design concepts requires the study of fatigue crack initiation and fatigue crack propagation stages at the notch root under realistic multiaxial loading scenarios [7–9].

Multiaxial fatigue is often treated as a problem involving complex external loadings that result in multiaxial stress-strain states [10–11]. Nevertheless, fatigue multiaxiality can arise not only from external loading but also from other factors, such as geometric discontinuities subjected to uniaxial load, residual stress fields, crack orientation, among others [12–13]. In fact, many engineering components are subjected to multiaxial loading, e.g. transmission shafts undergo combined bending-torsion, components of rotorcrafts experience bending-torsion, fixed-wing aircrafts also experience bending-torsion, just to mention a few. In these cases, since the crack propagates under mixed-mode loading conditions, the estimation of service life and the prediction of damage initiation are not trivial issues.

In the past few years, some effort has been put on the understanding of damage initiation and crack propagation in critical components subjected to bending-torsion [14–20]. Nevertheless, only a few studies have been focused on aluminium alloys [21–27]. Susmel et al. [21] examined the effect of loading biaxiality on crack patterns and crack propagation mechanisms in solid cylindrical specimens made of 6082-T6 aluminium alloy and found that crack initiation was mode-II dominated while crack propagation was mode-I governed. Singh et al. [22] studied the fatigue crack initiation and fatigue crack propagation mechanisms in tubular geometries made of 7075 aluminium alloy subjected to proportional loading. More recently, the same research team has addressed the effect of overloads on fatigue crack growth in cruciform specimens made of 7075 aluminium alloy [23–24].

The development of new predictive approaches to estimate the fatigue lifetime of aluminium alloy components under bending-torsion has been another topic of interest [25–29]. Abreu et al. [26] introduced a new energy-based approach to estimate the fatigue lifetime in welded tubular joints made of 6060-T6 aluminium alloys subjected to constant-amplitude and variable-amplitude loading. Kluger et al. [27] proposed a new critical plane model sensitive to mean stress effects to assess the

* Corresponding author.
E-mail address: ricardo.branco@dem.uc.pt (R. Branco).

https://doi.org/10.1016/j.ijfatigue.2022.106947
Received 11 February 2022; Received in revised form 24 March 2022; Accepted 21 April 2022
Available online 30 April 2022

durability of both 2017A-T4 and 6082-T6 aluminium alloys. Karolczuk et al. [28] studied the fatigue failure probability in 7075-T651 aluminium alloys by means of an improved life-dependent material parameter in conjunction with stress-based fatigue criteria.

The fatigue behaviour of notched components has generated considerable research interest. A recent comprehensive state-of-the-art review on the topic can be found in the reference [30]. The first approach on fatigue life assessment in notched members was formalised by Peterson who introduced the idea of average stress obtained in the vicinity of the geometric discontinuity [31]. This idea was the forerunner of the modern notch fatigue analysis theories implemented from the distribution of stress, strain, or energy parameters in a finite volume near the notch root [30]. Among them, the novel energy field intensity approach, recently introduced by Liao and Zhu [32], gathers the advantages of energy-based criteria with local gradient methods to account for the effective damage region.

The above-mentioned energy-based approach has been successfully implemented to estimate the fatigue life of notched components subjected to multiaxial loading using an elastic-plastic constitutive model [32]. Nevertheless, the application of this newly introduced concept by means of pseudo-elastic stresses can be of great interest since the analysis of engineering components is often conducted using linear-elastic simulations. This strategy can reduce the computational effort as well as the overall cost since these numerical models require a limited number of material constants and can be implemented in any commercial finite element package.

However, the development of such an approach needs an accurate computation of the cyclic plastic response at the notch root. Although, in theory, the elastic-plastic simulations are more precise, pseudo-elastic simulations have the advantage of being faster and simpler, because they do not require complex constitutive models, nor too much computational time, while providing high efficiency. These advantages may explain the popularity of the Neuber's rule and the Glinka's rule [33,34]. Even though the former tends to overestimate the notch root strains and the latter tends to underestimate the notch root strains, both have been successfully used in notch fatigue analysis under multiaxial loading [35] and will be used in the present research.

This paper studies the fatigue damage behaviour in notched cylindrical geometries made of 7050-T6 aluminium alloy subjected to proportional bending-torsion loading. In a first stage, the paper provides a comprehensive insight into the fatigue crack initiation and fatigue crack propagation processes associated with the normal stress to shear stress ratios. Then, fatigue crack initiation and fatigue crack propagation lives are distinguished based on the material characteristic length. After that, the fracture surfaces are analysed in order to identify the main failure modes as well as the fractographic features associated with the fatigue crack initiation and fatigue crack propagation regions. Finally, the energy field intensity concept is applied to estimate the fatigue life. The cyclic plastic response at the notch root is simulated using pseudo-elastic stresses along with local stress-strain approaches.

2. Materials and methods

2.1. Material

The material studied in this study was a high-strength 7050 aluminium alloy in the T6 condition (i.e. solid-solution treated and artificially aged) supplied in the form of a 30 mm-thick plate. This metallurgical state, characterised by a precipitation hardening mechanism, involves the formation of a fine dispersion of second phase particles that hinders the movement of dislocations leading to the maximum strength. Its nominal chemical composition as well as its main mechanical properties are summarised in Table 1 and Table 2, respectively.

The microstructure of the tested alloy in the transverse plane is shown in Fig. 1. As can be seen in the figure, it is composed by band-like grains aligned with the rolling direction and exhibits a certain degree of recrystallization. Micron-size globular-shaped and rod-shaped precipitates disperse around the grain and sub-grain boundaries are also visible along the material. The average grain size calculated by applying the linear intersection method taking into account a series of random lines parallel to the rolling direction was 183 μm [37].

Table 1
Nominal chemical composition (wt%) of the 7050-T6 aluminium alloy [36].

Si	Fe	Cu	Mn	Mg	Cr	Zn	Zr	Ti	Al
0.12	0.15	2.1	0.1	2.0	0.04	6.2	0.1	0.06	Rem.

Table 2
Monotonic mechanical properties of the 7050-T6 aluminium alloy [36].

Yield strength, σ_{YS} (MPa)	546
Tensile strength, σ_{UTS} (MPa)	621
Elongation, Δ(%)	14
Young's modulus, E (GPa)	71.7
Poisson's ratio, ν	0.33
Cyclic hardening coefficient, K′ (MPa)	728.7
Cyclic hardening exponent, n'	0.0512

Fig. 1. Optical micrograph of the high-strength 7050-T6 aluminium alloy in the transverse direction [37].

2.2. Multiaxial fatigue tests

The multiaxial fatigue testing campaign was carried using notched solid cylindrical geometries (see Fig. 2) machined from the material plate along the rolling (L-T) direction. The geometric discontinuity was drilled by CNC, using a spherical burr, and consisted of a 4-mm diameter and 2-mm depth blind hole (see Fig. 2(b)). The notch surface was tested as-machined, while the external cylindrical surface around the hole was polished by means of progressively finer silicon carbide papers (P600-grit, P1200-grit, and P2500-grit) followed by diamond paste.

The experimental tests were performed under proportional bending-torsion, at constant-amplitude load, with a stress ratio equal to 0, using sinusoidal waves and a cyclic frequency of 4 Hz. Three different bending moment to torsion moment (B/T) ratios were studied: B/T = 2/3, B/T = 1, and B/T = 2 (see Table 3). The crack detection and the crack growth at the notch region was monitored in-situ using a high-resolution digital camera connected to a PC-based data acquisition system. The tests were stopped when the crack in the outer cylindrical surface of the specimen reached a length greater than 4 mm. The total fatigue life (N_f) was calculated for a crack length of 3 mm while the crack initiation life (N_i) was calculated using a fracture mechanics criterion.

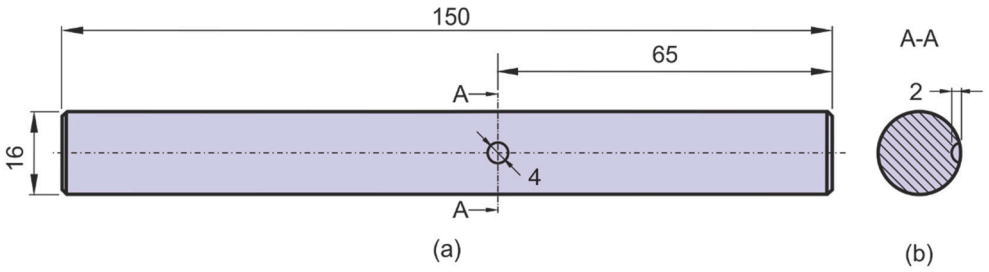

Fig. 2. Specimen geometry used in the multiaxial fatigue programme: (a) front view; (b) transversal cross-section (units: millimetres).

Table 3
Loading scenarios and nominal stresses of the multiaxial fatigue programme.

Test	B/T ratio	σ/τ ratio	Normal stress amplitude, σ_a (MPa)	Mean normal stress, σ_m (MPa)	Shear stress amplitude, τ_a (MPa)	Mean shear stress, τ_m (MPa)
1	2/3	4/3	134	140	100	105
2	2/3	4/3	107	113	81	85
3	1	2	134	146	67	73
4	1	2	107	116	54	58
5	2	4	172	186	43	46
6	2	4	134	143	34	36

2.3. Analysis of fracture surfaces

The fracture surfaces of selected specimens subjected to different B/T ratios were examined using a 3D coordinate measurement machine, Mitutoyo Quick Vision Apex 302, equipped with a programmable LED stage and coaxial lighting system. The fracture surface examination was conducted using a 2× magnification lens with a encoder scale type and a resolution of 0.1 μm. Topography data processing and calculations were done by means of MountainsMap surface metrology software. Surface textures were characterised by Abbott-Firestone curves constructed by finding the distribution of the heights of peaks and valleys in specific regions of the samples, namely crack initiation, crack propagation and final rupture areas. Fracture surfaces were also examined by scanning electron microscopy, using a Carl-Zeiss Gemini 500 FE-SEM model, to identify the main failure modes associated with the different loading scenarios.

2.4. Numerical simulations

The numerical simulations aimed to compute the stress-strain fields at the geometric discontinuities for the tested loading scenarios. The three-dimensional models were developed using 8-node brick elements assuming a homogeneous, isotropic, and liner-elastic behaviour. The mesh topology encompassed a ultra-fine region at the notch region where the stress gradients are stronger, and a coarser region in the remaining volume of the body to reduce the computational overhead (see Fig. 3). The minimum element size in the notch region had 70 μm side. The model contained 124,750 elements and 132,944 nodes. The elastic constants of the 7050-T6 aluminium alloy are presented in Table 2.

Regarding the gripping system (i.e. the prismatic bar and the larger cylindrical volume of Fig. 3) which was made of steel, the elastic constants were E = 210 GPa and $\nu = 0.3$. The bending moment to torsion moment ratios were generated from a single force, F, applied directly on the gripping system, whose point of application was defined in a case-by-case basis by changing the value of h (L was fixed). The griping system and the specimen were rigidly connected, while the outer surface of the other end of the specimen was fixed for an extension of 30 mm (see Fig. 3). A mesh convergence study was performed to define the refinement level in the notched region.

3. Results and discussion

This section is divided into four sections. The first section analyses the effect of the bending moment to torsion moment ratio on fatigue crack initiation and fatigue crack propagation responses. Next, the fatigue crack initiation and the fatigue crack propagation lives are

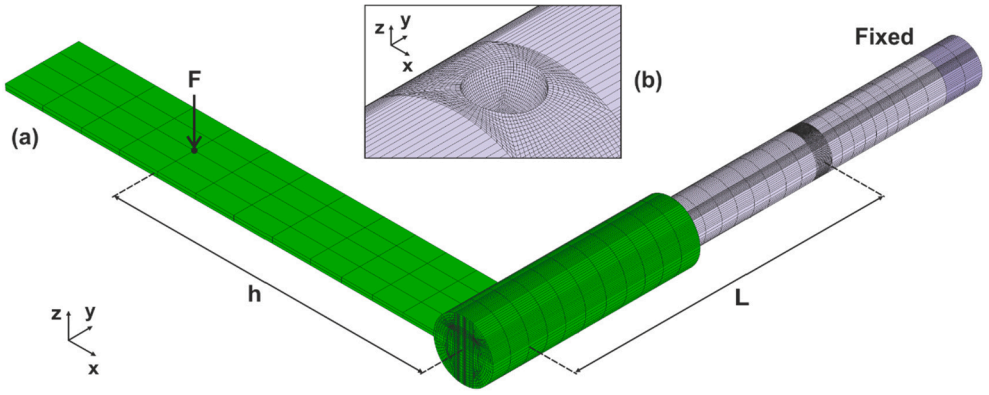

Fig. 3. Finite element mesh: (a) assembled model (124,750 elements and 132,944 nodes); (b) detail of the geometric discontinuity (notch radius: 4 mm; notch depth: 2 mm).

calculated by applying a fracture mechanics criterion. Then, fracture surfaces are examined to identify the main failure modes and to characterise the fractographic features. The last section focuses on the fatigue life estimation which is done by combining the energy field intensity concept with a local stress-strain approach used for the analysis of cyclic plasticity at the notch root.

3.1. Fatigue behaviour

An important issue in fatigue design is the identification *a priori* of the crack initiation sites. This complex problem is even more challenging when we are dealing with severe geometric discontinuities subjected to multiaxial loading. Fig. 4 summarises the crack initation process for the different cases examined in this study. The experimental observations are represented by the squares, while the circles represent the numerical predictions. Regardless of the loading case, two cracks nucleated in diametrically opposite sides of the hole surface. It is also clear that the fatigue crack initation process is governed by the multiaxial loading scenario. The crack initation sites tend to be closer to the hole border and closer to the x-axis, as the B/T ratio increases, which can be explained by the lower shear stress level.

The numerical predictions, represented by the circles in the pseudo-color views at the bottom part of Fig. 4, are in good agreement with the experimental observations. In this study, the fatigue crack initiation sites were defined as the surface nodes with maximum values of the first principal stress. This approach has been successfully used in previous studies focused on notched components made of high-strength steels subjected to in-phase bending-torsion loading [38]. The existence of local stress raisers at the hole surface, introduced by the drilling process, may be a possible reason for some deviations between the predicted coordinates and the experimental sites. However, the proposed approach is sensitve to the multiaxial loading scenario which is an important outcome.

The comparison between the experimental observations and the predicted results for the different loading cases was done quantitatively by accounting for the α angle defined as the angle formed between the x-axis and the straight line that connects the crack initiation node and the center of the hole (see Fig. 5(a)). The angles on the left side of the hole are identified by A, while the angles on the right side of the hole are identified by B. Overall, irrespective of the B/T ratio, there is a good correlation between both variables, with more than 90% of the points within scatter bands of ±10°, and with more than 80% of the points within scatter bands of ±5°. It is also visible that the crack angles at the early stage of growth decrease for higher values of B/T, which is explained by the lower shear stress level.

The prediction of the fatigue crack direction at the early stage of growth is fundamental information to better define inspection and maintenance tasks. However, in engineering components subjected to multiaxial loading, this is not a trivial issue. Fig. 5(b) compares the crack angles at the early stage of growth (β) measured at the initiation sites with those predicted numerically for the different loading cases. The angles on the left side of the hole are identified by A, while the angles on the right side of the hole are identified by B. The numerical predictions were done by accounting for the first principal direction at the crack initiation nodes [38]. The normal and shear stresses were determined in spherical coordinates using the numerical simulations.

Regarding the values of the β angles, see Fig. 5(b), the predicted values were also close to the experimental observations but the errors were higher than those of the initiation sites. In this case, only 50% of the points were within scatter bands of ±5°, and only 75% of the points were within scatter bands of ±10°. However, the proposed approach is able to satisfactorily capture the crack direction in this geometry when

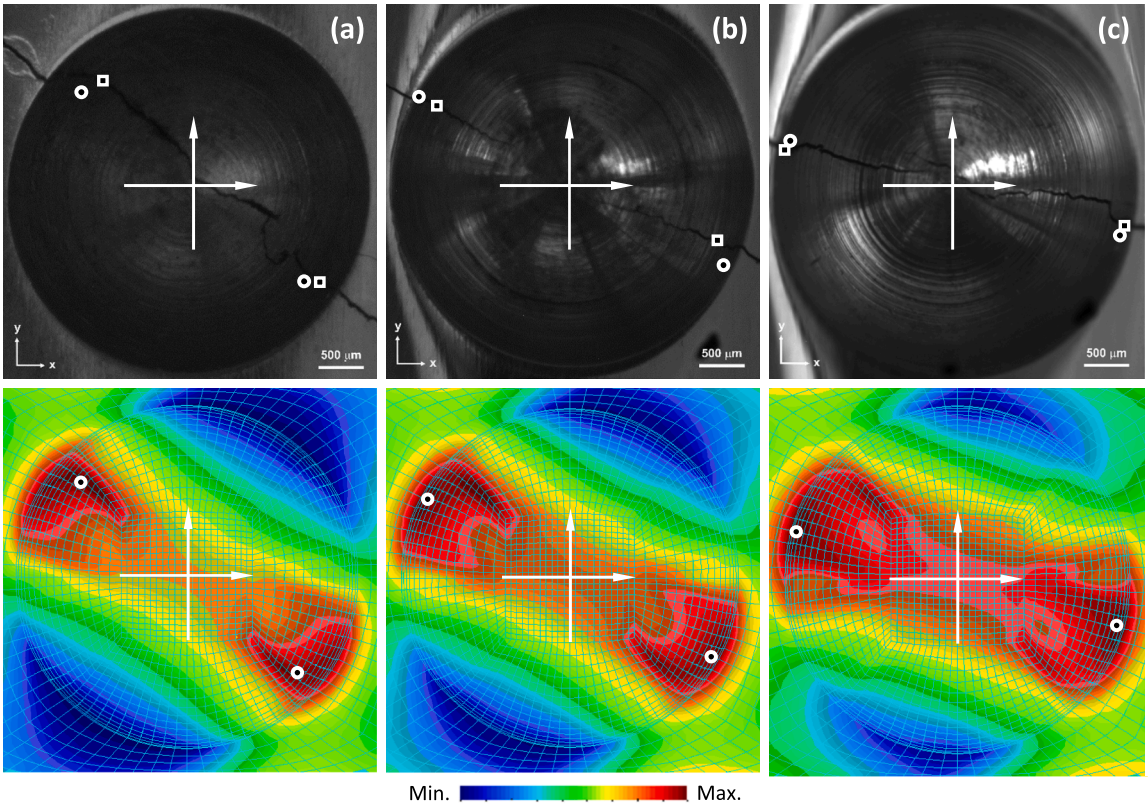

Fig. 4. Fatigue crack initiation sites: (a) B/T = 2/3; (b) B/T = 1; (c) B/T = 2. The circles denote the numerical predictions while the squares denote the experimental observations (the x-axis identifies the transversal direction and the y-axis identifies the longitudinal direction). The contour plots represent the first principal stress fields obtained in the numerical simulations.

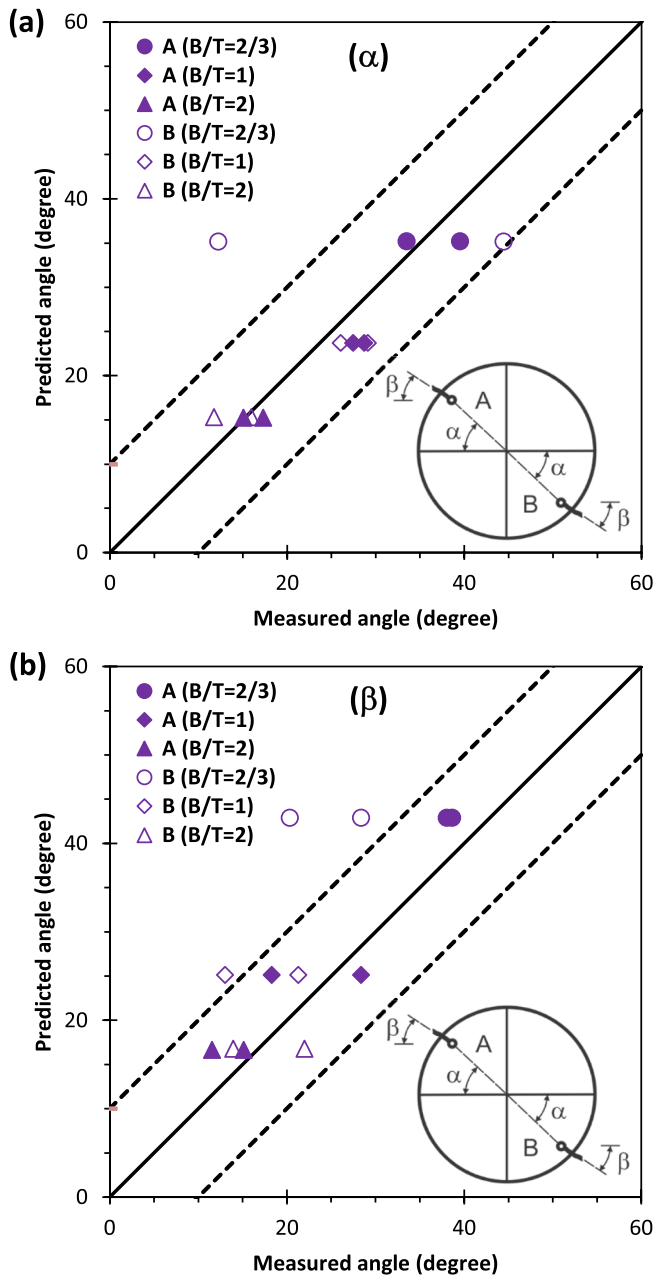

Fig. 5. Comparison of experimental observations and numerical predictions: (a) crack initiation sites (α); (b) crack initiation angles (β).

subjected to in-phase bending-torsion loading. In the literature, other approaches with similar level of accuracy have been employed [40–41]. Luo et al. [39] estimated the crack direction in thin-walled tubes with circular holes using a notch critical plane method, while Zerres et al. [40] computed the crack direction in notched tubular geometries via the maximum tangential stress theory.

It is also clear from Fig. 5(b) that the predictions for crack A were better than those for crack B. In the former case, the maximum differences varied between 3° and −7° (i.e. all points were within the scatter bands of ±10°) while in the latter the values were more randomly spread out. A plausible explanation for this behaviour may be associated with the instant at which the second crack initiated. When it occurred after a small number of cycles, both cracks appeared in almost diametrically opposite locations without significant loss of stiffness. On the contrary, when the second crack initiated later, the residual stiffness was affected, slightly changing the initiation process and, thus, the crack direction. In such a case, the proposed approach, which is based on an uncracked body, seems to be less accurate.

Another conclusion is that the β angles decrease for higher B/T ratios (see Fig. 5(b)). Indeed, in the absence of shear stresses, the crack is subjected to mode-I loading and, predictably, it tends to advance in a direction normal to the main axis of the specimen (β = 0°). The increase of the shear stress level, i.e. the reduction of the B/T ratio, leads to a higher degree of mixed-mode loading and an increase in the crack angle at the early stage of growth. It can be also concluded that the predictions of crack direction for both sides of the hole are similar (see Fig. 5(b)). The maximum differences in the tested cases were lower than 0.1°. This can be explained by the symmetry of the stress fields, as can be distinguished in Fig. 4.

The knowledge of the fatigue crack paths in engineering components subjected to cyclic loading is pivotal to understand whether a potential failure is benign or catastrophic. In this geometry, the fatigue process, as already discussed, is strongly dependent on the loading scenario. As far as the surface crack paths are concerned, we can note that the trajectories tend to be closer to the x-axis for higher B/T ratios (see Fig. 4). Higher B/T ratios reduce the predominance of the shear stress level, and, therefore, the crack fronts tend to propagate closer to pure mode-I. Another common feature observed in the experiments is the existence of crack paths with some serration. The as-machined condition of the hole introduces local randomly stress raisers which may deviate the trajectory.

Fig. 6 plots the so-called a-N curves, i.e. the relationship between the surface crack length (a) and the number of loading cycles (N), for different B/T ratios and loading levels. The surface crack length was measured using the images collected periodically during the tests. Here, only the results of the first crack detected in the hole surface are presented. The a-N curves were governed by the stress level and the bending moment to torsion moment ratio. The former effect can be inferred by comparing the cases tested under the same B/T ratio but different nominal stresses, see for instance the circle series, or the triangle series, or the diamond series. In any case, we can observe that higher stress levels speed up the fatigue crack initiation process and increase the curve slopes for the same crack length.

In relation to the latter effect, we can take some conclusions from the analysis of the series tested under the same stress amplitude (σ_a = 134 MPa) but with different bending moment to torsion moment ratios (see the three series on the left of Fig. 6). Except for the case B/T = 2, we can see that the fatigue crack initiation is faster for higher shear stress levels (despite the series B/T = 2 behaves differently, this slightly incoherency can be attributed to the scatter nature of the fatigue phenomenon). In a second stage of the test, for a crack length greater than 1.25 mm, we can observe the expected trends, i.e. the slopes for a fixed crack length decrease with the increase of the B/T ratio, which can be explained by the reduction of the shear stress level.

3.2. Experimental fatigue life

In this section, the fatigue crack initiation and the fatigue crack propagation lives are distinguished using fracture mechanics concepts. The definition of the crack length that distinguishes the two above-mentioned stages encompasses some philosophical debate [39]. In part this is because there is no clear boundary between an uncracked material and a cracked material, which makes difficult to judge whether or not a crack exists. Nevertheless, the use of an objective approach based on the crack length seems to be a reasonable and feasible strategy to distinguish fatigue crack initiation from fatigue crack propagation [41]. Here, this distinction is established using the El-Haddad's empirical equation, defined as follows [42]:

$$a_0 = \frac{1}{\pi}\left(\frac{\Delta K_{th}}{\Delta \sigma_0}\right)^2 \quad (1)$$

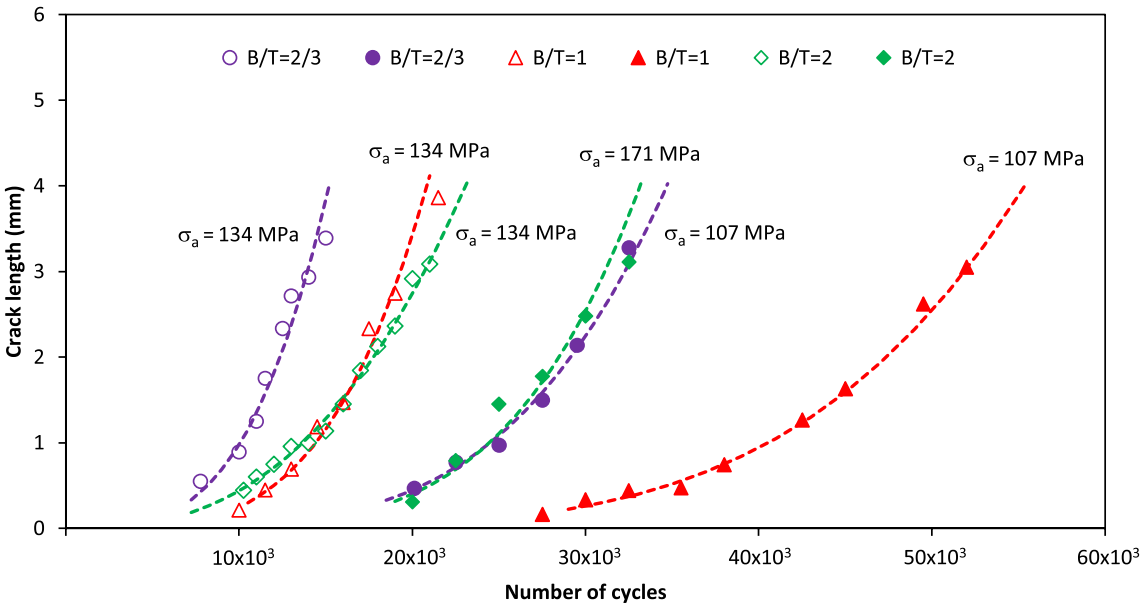

Fig. 6. Surface crack length versus number of loading cycles for different bending moment to torsion moment ratios and stress amplitudes. The crack length was measured from the images collected in the experiments for the first crack detected in the hole surface. The data points were fitted using power functions.

where ΔK_{th} is the stress intensity factor range threshold, and $\Delta\sigma_0$ is the fatigue limit stress range, which must be estimated for the stress ratio of the notched component. The values of the two constants for the high-strength 7050-T6 aluminium alloy subjected to pulsating loading conditions ($R = 0$) were determined from previous studies carried out by the research group of the authors [36,43] for which the value of a_0 was equal to 249 μm. The fatigue crack initiation life (N_i) for the different tested cases was computed using the a-N curves exhibited in Fig. 6 that refer to the first crack detected in the hole surface. The total fatigue life (N_f) was estimated in a similar manner, also using the a-N curves, for a final crack length equal to 3 mm. The values found for the various multiaxial scenarios are summarised in Table 4.

The relationship between the fatigue crack initiation life (N_i) and the total fatigue life (N_f) for the tested cases is plotted in Fig. 7. As can be seen in the figure, irrespective of the B/T ratio or the stress amplitude, the N_i/N_f ratios are relatively similar for all tests, varying in the range 39–57% with an average value of 51% and a standard deviation of 6.4%. These values are relatively close to those reported in the literature ($42\% \leq N_i/N_f \leq 73\%$) by Branco et al. [44] for solid round bars with lateral U-shaped notches subjected to proportional bending-torsion loading. However, in this latter study, the fatigue crack initiation process was more complex, showing either the nucleation of a single crack or the nucleation of multiple cracks, which may explain the wider interval.

Another way to examine the life fraction in terms of fatigue crack initiation and fatigue crack propagation is via the N_i/N_p ratio (where N_i represents the fatigue crack initiation life and N_p represents the fatigue crack propagation life). Here, the fatigue crack propagation life was estimated by subtracting the fatigue crack initiation life from the total fatigue life. In general, this ratio is quite sensitive to the extent of each fatigue stage. The N_i/N_p ratios varied between 64 and 137% with an average value of 108% and a standard deviation of 25%. In other words, the crack initiation stage was generally longer than the crack propagation stage and the former stage had a duration in the range 2/3 to 4/3 of the crack propagation stage.

Table 4
Experimental and predicted fatigue lives.

Test	Crack initiation life, N_i (cycles)	Total fatigue life, N_f (cycles)	Predicted life via Glinka's rule, $N_{p,G}$ (cycles)	Predicted life via Neuber's rule, $N_{p,N}$ (cycles)
1	6663	13,952	4720	5771
2	17,290	32,275	9364	9461
3	9994	19,311	15,350	15,446
4	29,709	51,882	54,060	51,729
5	8082	20,705	5567	5867
6	18,026	31,120	10,056	10,071

Fatigue design models are often established using stress-life approaches. This is because damage quantifiers based on stress parameters correlate well with fatigue life. Fig. 8 plots the fatigue crack initiation life (N_i) against the nominal equivalent von Mises stress amplitude ($\sigma_{a,vMn}$) for the different multiaxial scenarios on log-log scales (see the purple filled-in circles). As far as can be seen, there is some scatter between both variables which means that this approach is not able to properly account for the notch effect for this geometry under the studied loading scenarios. In the same way, the correlation between the total fatigue life (N_f) and the nominal equivalent von Mises stress amplitude ($\sigma_{a,vMn}$) displayed by the green filled-in diamonds is also not particularly relevant. Thus, a reliable fatigue design approach needs the identification of a reliable fatigue damage quantifier.

Fig. 8 plots the fatigue crack initiation life (N_i) against the local equivalent von Mises stress amplitude ($\sigma_{a,vML}$) for the different studied cases on log-log scales (see the circles outlined in purple). The latter variable was computed using the numerical models and corresponds to the equivalent von Mises stress amplitude at the crack initiation node (see Fig. 4). It is clear from the figure that this parameter, already introduced in previous studies available in the open literature, allows to capture the relationship between the loading scenario and the fatigue crack initiation life [35,38,44]. Two fatigue design bounds, represented by the upper and lower straight lines, were drawn for a 95% survival probability calculated from the mean curve assuming two-sided confidence levels equal to 75%. As can be seen in the figure, the value of the scatter index is relatively small.

The local von Mises stress amplitude is also capable of correlating the multiaxial loading scenario with the total fatigue life (N_f). Overall, as can be seen in Fig. 8, there is a good correlation between $\sigma_{a,vML}$ and N_f for the different cases. In fact, the coefficients of determination (r^2) of the mean curves are relatively similar, more specifically 0.874 and 0.863 for the $\sigma_{a,vML}$-N_f and $\sigma_{a,vML}$-N_i functions, respectively. Although the difference is not significant, it is well accepted that fatigue crack initiation is

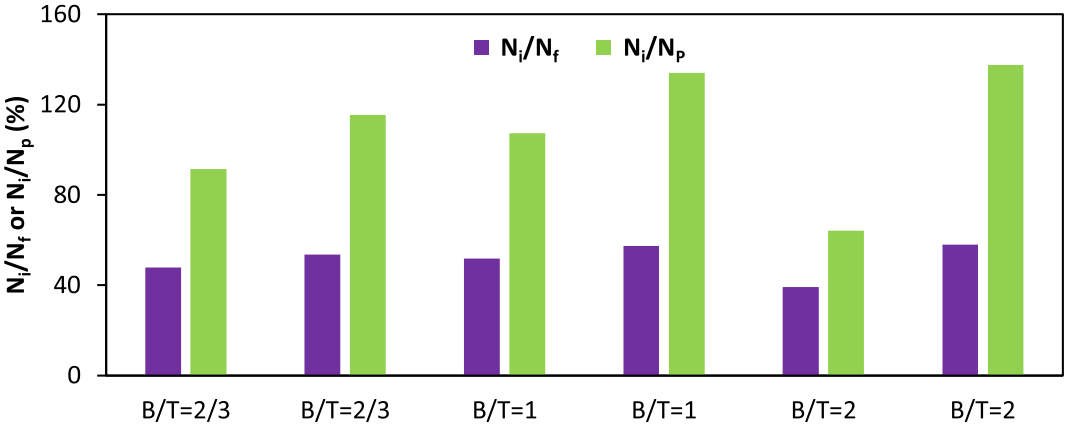

Fig. 7. Variation of the N_i/N_f ratio and the N_i/N_p ratio for the different loading cases.

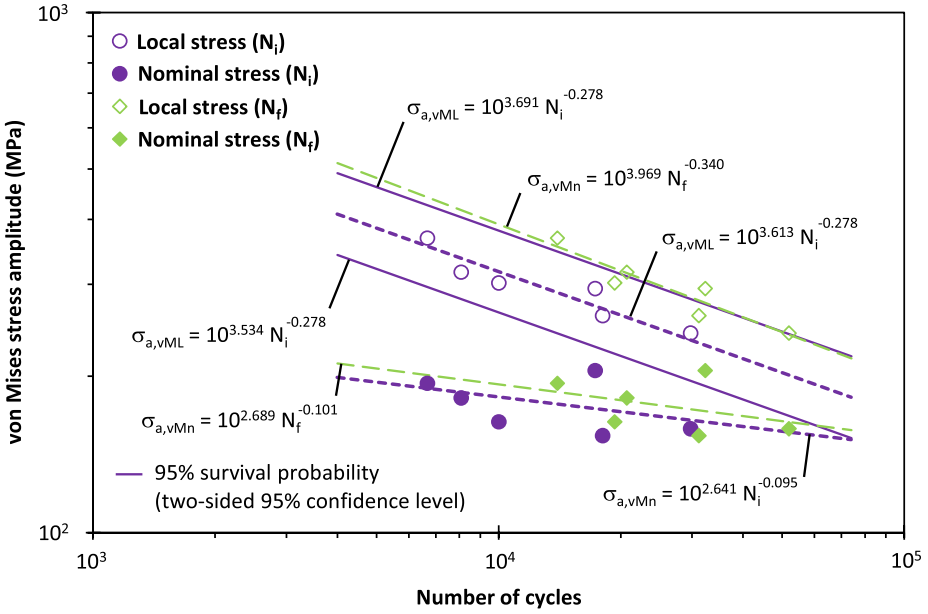

Fig. 8. Stress-life relationships for the tested cases based on nominal and local stresses. Fatigue life is accounted for in terms of crack initiation life (N_i) and total fatigue life (N_f). Stress is accounted for using the nominal von Mises stress amplitude ($\sigma_{a,vMn}$) and local von Mises stress amplitude ($\sigma_{a,vML}$).

associated with a higher scatter, which may explain the better correlation for the total fatigue life. Another interesting outcome is the fact that the slopes of the two above-mentioned functions were relatively different (i.e. −0.340 and −0.278) while those obtained from the nominal equivalent von Mises stress were quite similar (i.e. −0.101 and −0.095).

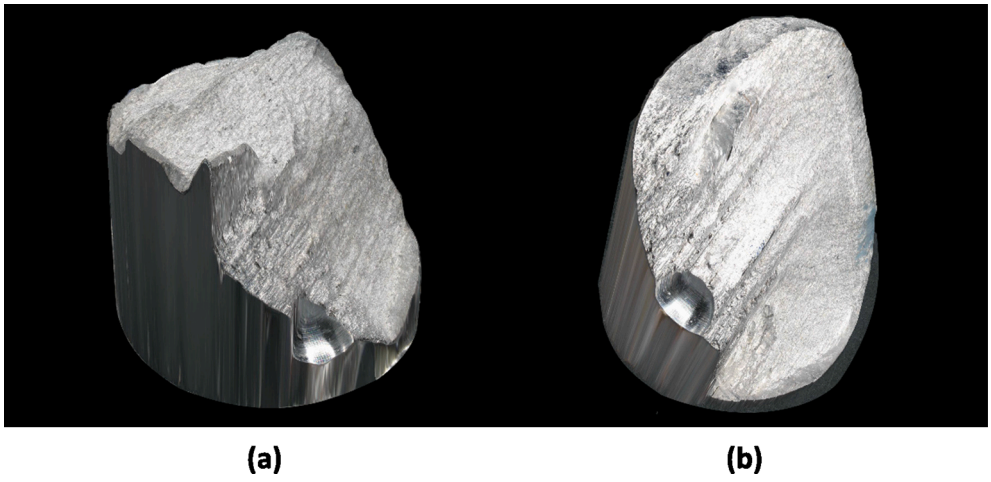

Fig. 9. Three-dimensional fracture surface topologies acquired via optical focus-variation microscopy: (a) B/T = 2/3; (b) B/T = 2.

3.3. Fracture surface morphology

Fig. 9 displays two examples of the typical fracture surface topologies obtained for this geometry when subjected to bending-torsion loading. In these two cases, the cracks propagated until the total failure of the specimens (and not until a crack length of 4 mm) to better understand the effect of multiaxiality on fracture surface topologies. At the first sight, it is clear that the fracture surface topologies are rather complex, either for higher shear stress levels (Fig. 9(a)), or for lower shear stress levels (Fig. 9(b)). The fracture surface is the result of a propagation in multiple planes with increasingly higher slopes, as the B/T ratio decreases. The higher shear stress levels associated with lower B/T ratios increase the mixed-mode degree along the crack front resulting in more curved surfaces.

A close analysis of the fracture surface topology in the crack initiation region (Fig. 10(a)) and crack propagation region (Fig. 10(c)) via optical focus-variation microscopy evidences a considerable variation of the fractographic features during the crack growth process. As can be seen in the pseudo-colour views, which show the height variation from the minimum z-axis coordinate, the surface roughness increases, as the crack propagates. At the crack initiation region, see Fig. 10(a), the interval of variation of the surface roughness values is smaller and varies through the surface in a smooth manner. In contrast, at the crack propagation region, see Fig. 10(c), the variations are more significant and tend to be more randomly distributed throughout the surface leading to higher levels of asperity.

This behaviour can be explained by the successively higher levels of plastic deformation underwent by the material due to the reduction of the uncracked cross-section of the specimen. The histograms of the height distribution and the Abbott-Firestone curves confirm this fact: the crack initiation regions (Fig. 10(a)) have higher frequency peaks in the middle range of the histogram, while in the crack propagation region (Fig. 10(c)) the higher frequency peaks are disperse throughout the entire histogram without a clear distribution trend which can be caused by the higher fatigue crack growth rates associated with this region. This different behaviour is highlighted in cumulating functions of the depth

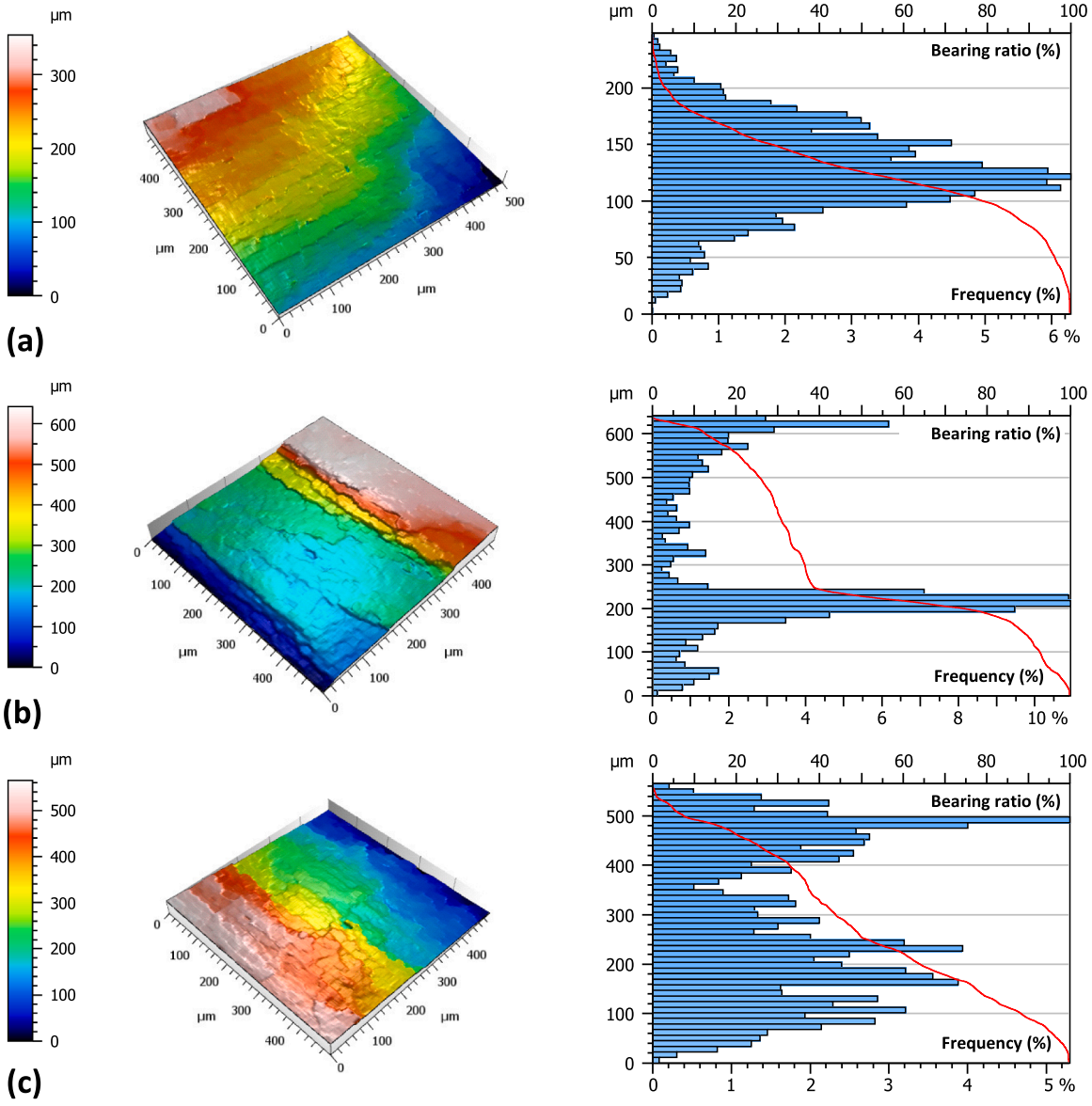

Fig. 10. Pseudo-color views and Abbott-Firestone curves obtained for the of the height distribution from the minimum z-axis coordinate for: (a) the crack initiation region; (b) junction of cracks; (c) crack propagation region.

distribution represented by the red curves. In the case of the crack initiation region, the curve increases rapidly in the intermediate region, while in the crack propagation region the curve is almost linear.

Fig. 10(b) shows the fractographic features of a region where two cracks met and coalesced. The red area of the pseudo-colour view identifies the fatigue step formed during the junction of both cracks while the remaining area displays the fracture surface of one crack before the coalescence. As can be seen in the figure, there is a clear contrast between the two above areas; the height values change abruptly when the two cracks met, as reflected by the Abbott-Firestone curve (see the red curve). Although the highest frequency peaks appear in the range 200–240 μm (which are close to those reported for the crack initiation region) we can also find relevant frequency peaks in the range 600–700 μm.

The examination of the fracture surfaces by scanning electron microscopy (SEM) has confirmed that the fatigue crack initiation process is characterised by the nucleation of two cracks in two opposite sides of the hole but close to the outer cylindrical surface. This is clearly visible in the overview images of the fracture surface near the hole region for the loading cases B/T = 2 (Fig. 11(a)) and B/T = 2/3 (Fig. 11(b)) where the fatigue crack initiation sites are identified by the arrows. This behaviour agrees with the numerical predictions (see Fig. 4) which suggests that initiation occurs in two diametrically opposite locations near the border of the hole but in the spherical surface.

Another interesting finding is that the positions of the fatigue crack initiation sites are affected by the multiaxial loading scenario and tend

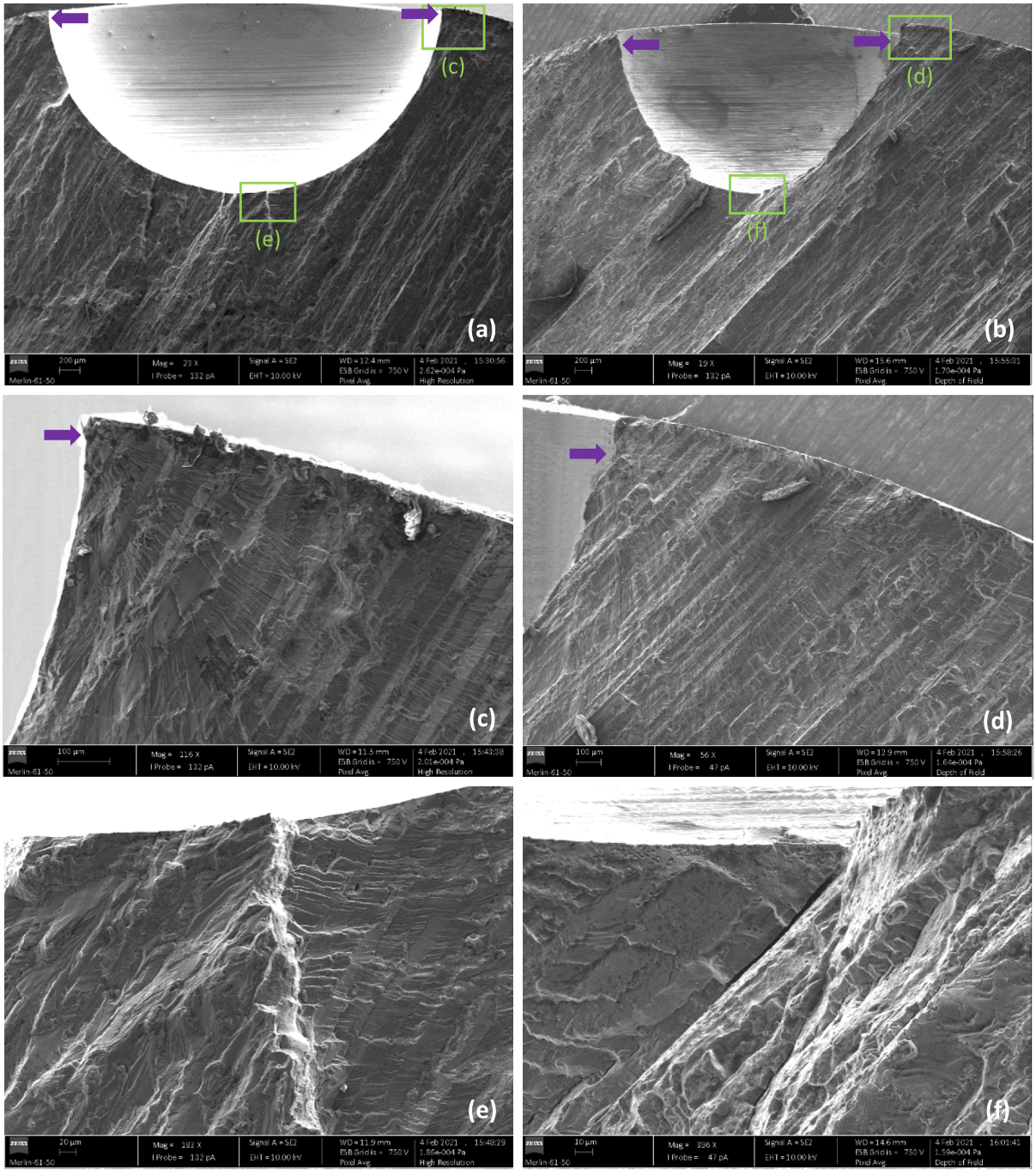

Fig. 11. SEM images of the fracture surfaces. General overview of the hole region for: (a) B/T = 2 and (b) B/T = 2/3; detailed view of the initiation site for: (c) B/T = 2 and (d) B/T = 2/3; fatigue step caused by coalescence of multiple cracks for: (e) B/T = 2 and (f) B/T = 2/3. The arrows represent the fatigue crack initiation sites.

to approach the outer cylindrical surface, as the B/T ratio increases. This fact can be clearly distinguished in the detailed views of the fatigue crack initiation regions of the left side of the samples, taken with the same magnification, for the loading cases B/T = 2 (Fig. 11(c)) and B/T = 2/3 (Fig. 11(d)). It can be concluded that the fatigue crack initiation sites, identified by the arrows, move to more interior regions, as the shear stress level increases. These results also agree with the conclusions drawn from the numerical simulations (see Fig. 4).

The analysis of the fracture surfaces can provide important clues on the failure mechanisms associated with the fatigue crack initiation and fatigue crack propagation stages under various multiaxial loading conditions. The examined samples (see Fig. 11(a)-(d)) exhibited a number of distinct features of cleavage fracture in the region of fatigue crack initiation, such as river patterns, cleavage steps, feather marks, facets, and serpentine glides, suggesting a brittle nature of fracture [45–46]. Furthermore, Fig. 11(c) and Fig. 11(d) show that the cleavage fractures initiated on multiple cleavage lines forming a river pattern with radial convergence to the initiation sites. These pictures also reveal highly tortuous paths mainly formed by cleavage steps spread across the entire region.

The fatigue steps resulting from the coalescence of the two cracks for the loading cases B/T = 2 and B/T = 2/3 are shown in Fig. 11(e) and Fig. 11(f), respectively. In both cases, as can be seen in Fig. 11(a) and Fig. 11(b), the interception of the two propagation planes occurred near the deepest point of the hole surface, which may suggest that the two cracks initiated for a similar number of loading cycles and propagated with identical fatigue crack growth rates. Moreover, we can see in these magnified pictures the existence of secondary cracks with variable length in areas close to the fatigue step. This is particularly evident in the case of Fig. 11(e).

The fractographic features of fatigue crack propagation stages can be observed in Fig. 12. Irrespective of the loading scenario, we can clearly see the presence of cleavage steps along with fatigue striation marks partially developed in localised regions. The highly-magnified pictures also show that the fatigue striations suffer some annihilation. This behaviour suggests that the crack propagates in a dominant mixed-mode condition. It can also be seen that the variations of the local stresses, and possibly the microstructural changes, alter the orientation of fracture planes as well as the direction of fatigue striations. Moreover, multiple secondary cracks are also found which may result from the interaction of inclusions with the propagation striations [22].

3.4. Multiaxial fatigue life assessment

Fatigue life assessment of notched components is a challenging task. The current methodologies are generally based on different design philosophies which may include nominal stress-strain approaches, local stress-strain approaches, critical distance approaches, and energy-based approaches [47–55]. The two last groups are among the most popular because of their versatility to deal with complex geometric discontinuities and multiaxial loading histories. In this study, we apply the model proposed by Liao and Zhu [32] based on the sophisticated concept of Energy Field Intensity (EFI). Nevertheless, in the current approach, the model is formalised using a linear-elastic framework in conjunction with a local stress-strain approach [33–34].

The above-mentioned approach can be divided into two tasks. The first is focused on the material characterisation and the main goal is the development of a fatigue master curve relating the total strain energy

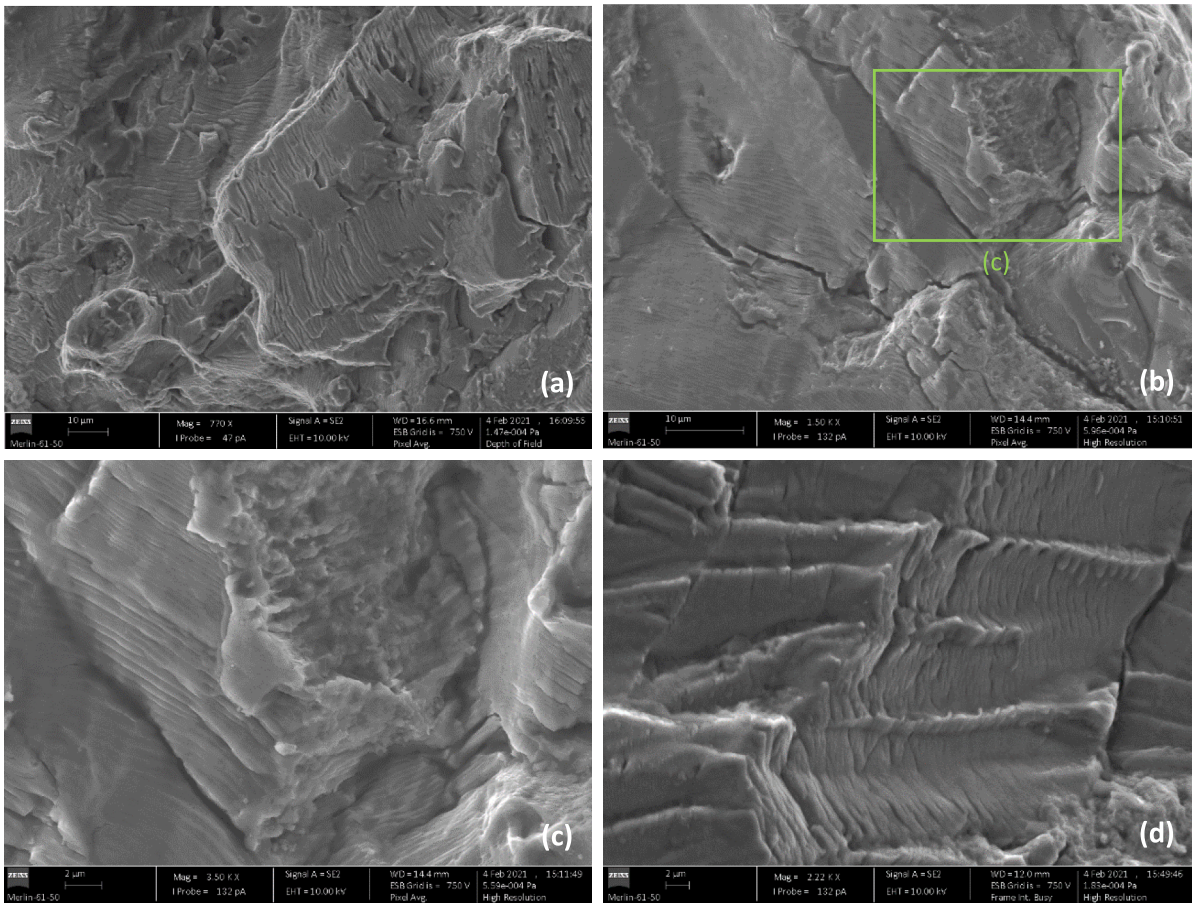

Fig. 12. High magnification micrographs of fracture surfaces: (a) B/T = 2/3; (b) B/T = 1; (c) B/T = 1; (d) B/T = 2.

density to the number of cycles to failure. This energy-life function is generally materialised by means of a series of strain-controlled tests performed using standard smooth specimens [56]. The fatigue master curve for the 7050-T6 aluminium alloy, determined in a previous study by the authors, is exhibited in Fig. 13 [36]. The tests were conducted under strain-controlled conditions for strain amplitudes (ε_a) in the range 0.5–1.75% and strain ratios (R_ε) of −1, 0, and 0.5. The fitted function for $R_\varepsilon = 0$ is shown in the figure.

The second task is devoted to the assessment of the fatigue crack initiation life of the notched geometries. Firstly, the multiaxial stress-strain state (see Fig. 14(a)) is reduced to an equivalent uniaxial stress-strain state via the equivalent von Mises stress (see Fig. 14(b)). The pseudo-elastic stress fields (represented by the L.E. function) are used to generate a series of hysteresis loops along the nodes near the notch root by applying a local stress-strain (LSS) method (e.g. Neuber's rule, Glinka's rule, etc.). Fig. 14(c) plots an example of the generated hysteresis loop for the von Mises stress range of the i^{th} node of Fig. 14(b).

The previous step allows the computation of the elastic-plastic stress fields (represented by the E.P. function) and also the distribution of the total strain energy density at the geometric discontinuity (see Fig. 14 (d)). Here, $\Delta W_T(r))$ is defined by the sum of both the plastic (ΔW_p) and the elastic positive (ΔW_e^+) components. Based on the above energy distribution, an effective value of the total strain energy density ($\Delta W_{T,eff}$) is computed taking into account the total strain energy density gradient ($\chi(r)$) represented in Fig. 14(d). Finally, the fatigue life is determined by inserting an effective value of the total strain energy density ($\Delta W_{T,eff}$) into the fatigue master curve of the tested material (see Fig. 14(e)).

The effective value of the total strain energy density in the vicinity of the notch is computed by accounting for the influence of the total strain energy density gradient, i.e.

$$\Delta W_{T,eff} = \frac{1}{r_{eff}} \int_0^{r_{eff}} \Delta W_T |1 - r\chi(r)| dr \quad (2)$$

$$\chi(r) = \frac{1}{\Delta W_{T,max}} \frac{d(\Delta W_T)}{dr} \quad (3)$$

where ΔW_T is the total strain energy density function associated with the external fatigue load, $\chi(r)$ is the total strain energy density gradient, and r_{eff} is the radius of the damage zone given by the distance between the minimum value of the total strain energy density gradient function and the notch tip. Detailed information about this highly efficient model can be found in the recent paper by Liao et al. [32].

Fig. 15 shows, as an example, the distribution of the pseudo-elastic equivalent von Mises stress in the vicinity of the notch determined from the linear-elastic numerical simulations. The figure also plots the elastic-plastic von Mises stress distributions obtained by applying the two local stress-strain approaches used in this study, namely the Neuber's rule, and the Glinka's rule. As can be seen, the pseudo-elastic equivalent von Mises stress is maximum at the notch tip, decreasing gradually to an asymptotic value. The application of the two local stress-strain approaches, as expected, corrects the stress profiles close to the geometric discontinuity but does not affect the stress distributions in regions far from the notch tip. Another interesting finding is that the two functions are similar, except in a small extent near the notch surface.

The functions of the total strain energy density computed from the elastic-plastic stresses with the two local stress-strain approaches are also plotted in Fig. 15. As referred to above, the total strain energy density was determined by the sum of both the plastic and the elastic positive components (see Fig. 14(c)). It is clear from the figure that the two approaches, in this case, lead to very similar energy distributions (see the circle series) since both curves are overlapped. A closed look at the figure shows that the values near the notch root are slightly higher for the Glinka's rule than for the Neuber's rule. The differences between the two functions increase for higher values of the applied stress level. It should be highlighted that similar trends were also found in the other cases analysed in this study.

Fig. 16 displays the typical total strain energy density gradients in the direction of the maximum total strain energy density obtained with the two local stress-strain approaches employed in this study. At the first sight, we can see that, irrespective of the local stress-strain approach, the functions of the total strain energy density gradients are similar. Therefore, this means that the radii of the damage zones (r_{eff}) are also identical. Moreover, it is clear that the energy gradients are higher near the vicinity of the notch than in remote positions. This indicates that the points closer to the geometric discontinuity, where the total strain energy density is also higher, contribute more to the fatigue crack initiation process than the points in remote positions. These trends were also

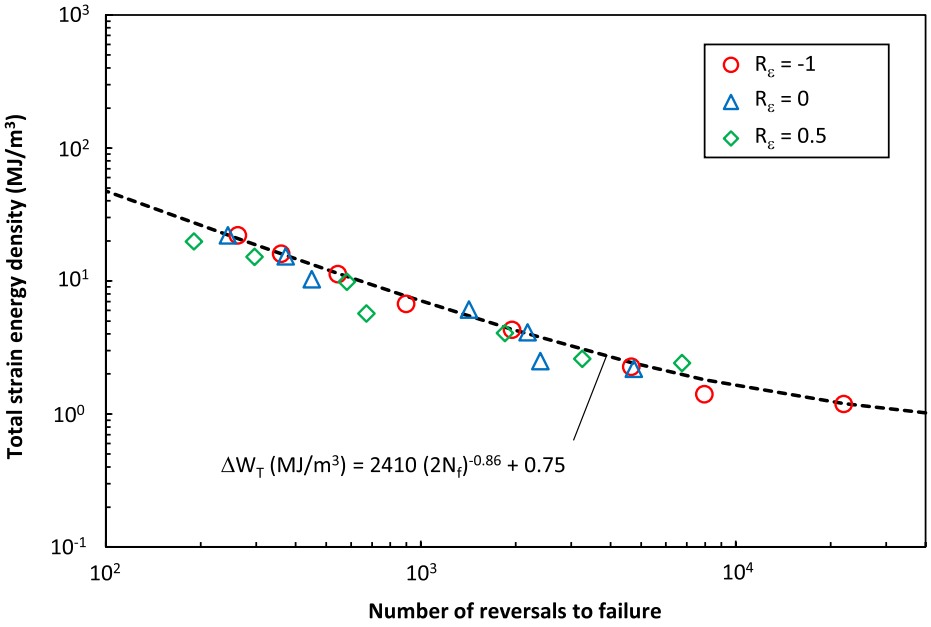

Fig. 13. Total strain energy density versus number of reversals to failure obtained from smooth samples subjected to uniaxial strain-controlled conditions for different strain ratios (R_ε).

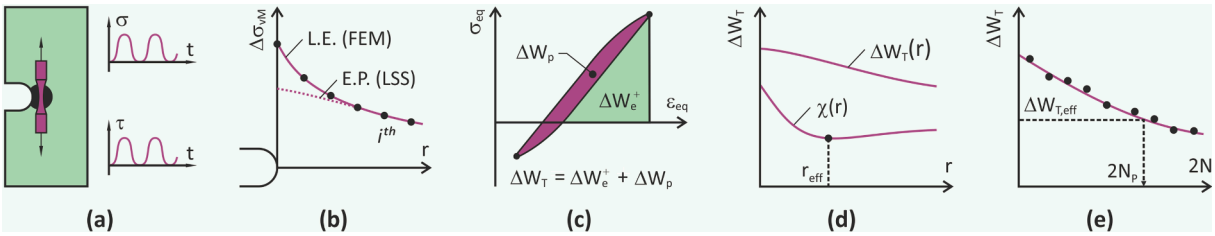

Fig. 14. Main steps of the fatigue life assessment model: (a) multiaxial loading scenario; (b) reduction of multiaxial stress state to an equivalent uniaxial stress state (L.E. represents the linear elastic distribution while E.P. represents the elastic–plastic distribution obtained with a local stress–strain approach); (c) generation of a representative hysteresis loop for the ith node along the notch root; (d) computation of the distribution of the total strain energy density ($\Delta W_T(r)$) in the vicinity of the notch and calculation of corresponding energy gradient ($\chi(r)$); (e) prediction of fatigue life.

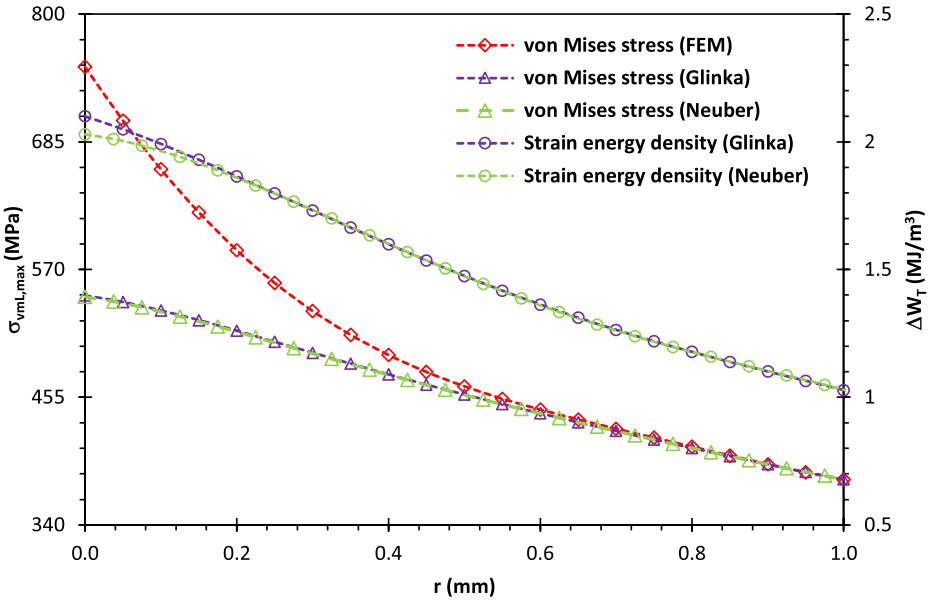

Fig. 15. Distribution of the maximum von Mises equivalent stress and the total strain energy density with the distance from the notch tip for B/T = 2/3 in the direction of maximum value of the total strain energy density.

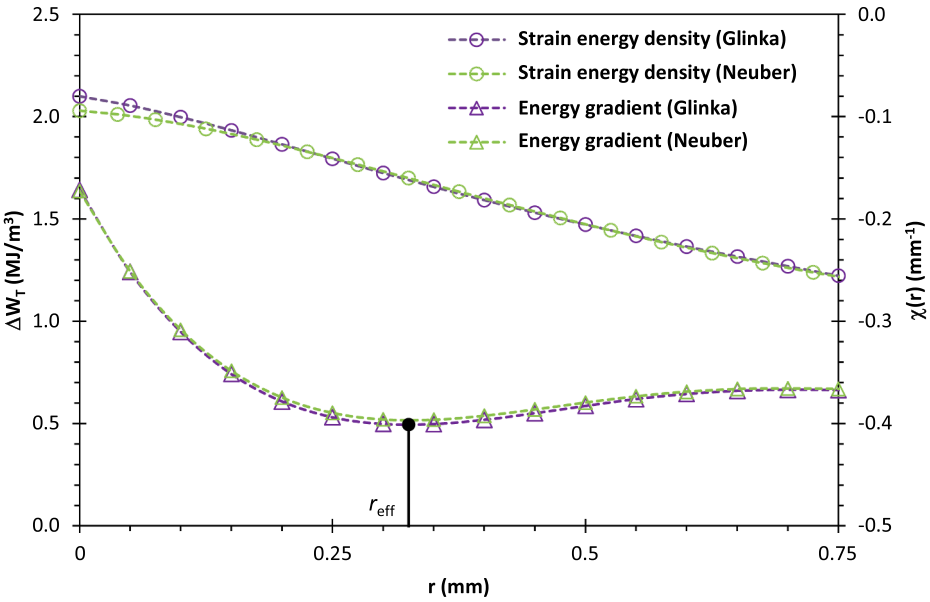

Fig. 16. Distribution of the total strain energy density with the distance from the notch tip for B/T = 2/3 in the direction of maximum value of the total strain energy density and the corresponding functions of the total strain energy density gradient.

found for the other cases considered in this study.

The analysis of Fig. 16 allows the identification of two obvious stages: a first region, close to the notch root, where the total strain energy density gradient drops rapidly; followed by a second region with almost stabilised values. A simple manner to divide these regions is by using the radius of the damage zone (r_{eff}) which corresponds to the minimum value of the strain energy density gradient function (i.e. $\chi(r) = -0.401\ mm^{-1}$ for $r_{eff} = 0.325$ mm). In the first region, the stress-strain concentration effects are more serious and, therefore, the total strain energy density gradients are more significant. It is interesting to note that the value of the total strain energy density corresponding to the minimum value of the strain energy density gradient is nearly equal to 80% of the total strain energy density that exists at the notch tip.

Finally, by inserting the effective values of the total strain energy density of the different loading cases into the fatigue master curve of the 7050-T6 alloy, see Fig. 14(e), we are able to estimate the fatigue crack initiation life (N_p). Fig. 17 plots the numerical predictions against the experimental results (N_i) for the different multiaxial loading cases and the two local stress-strain approaches (circle and rectangle series). The calculated values for the Glinka's rule ($N_{p,G}$) and the Neuber's rule ($N_{p,N}$) are listed in Table 4. For the sake of comparability, safe and unsafe scatter bands with factors of two (i.e. $N_e = 2N_p$ and $N_p = 2N_e$) were plotted in the figure. Overall, the fatigue lives predicted using the proposed approaches correlate well with the experimental observations.

A detailed analysis of the figure shows that the two models led to safe and unsafe results, but with more points shifted to the safe region. In addition, it is worth to note that all points, either for the Neuber's rule or for the Glinka's rule, were within scatter bands with factors of two (dashed straight lines). Comparing the two approaches, we can conclude that the predictions are very similar and that the Neuber's rule is slightly less conservative than the Glinka's rule. The analysis of the fatigue life prediction error, defined as the logarithm of the N_p/N_e ratio (i.e. Log N_p/N_e), shows that the mean error (γ) was higher for the former ($\gamma_{Neuber} = -0.0477$) than for the latter ($\gamma_{Glinka} = -0.0642$) which agrees with the previous conclusions. Regarding the standard deviation (η), the values also were rather consistent ($\eta_{Neuber} = -0.2171$ and $\eta_{Glinka} = 0.2287$) reinforcing the robustness of the proposed methods.

To conclude this section, we would like to highlight that the proposed approaches are capable to provide good correlations in terms of fatigue crack initiation life, as demonstrated above, but they are conservative in terms of total fatigue life. As can be seen in Fig. 17, see the triangle and diamond series, if we correlate the predicted fatigue lives (N_p) with the total fatigue life (N_f), which was calculated for a crack length equal to 3 mm, irrespective of the method used in the analysis, all points are moved to the safe side. This cannot be necessary negative but, in most of cases, such a translation is excessive, leading to too high safety factors.

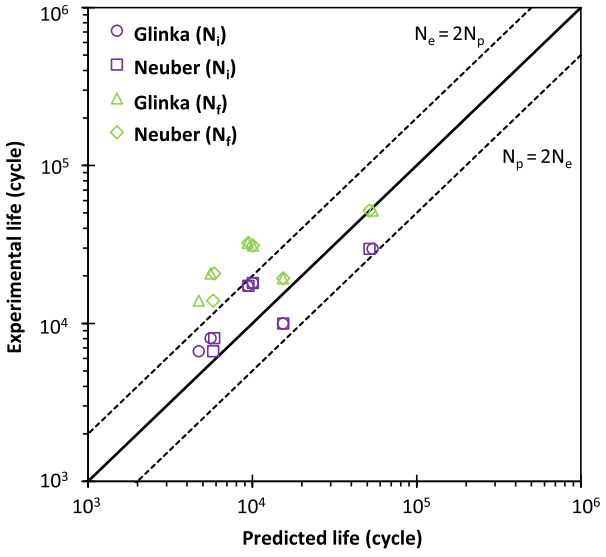

Fig. 17. Comparison of predicted and experimental fatigue lives for the tested cases.

4. Conclusions

The present paper studied the fatigue crack initiation and fatigue crack propagation behaviour of cylindrical bars with a lateral hole made of 7050-T6 aluminium alloy under multiaxial bending-torsion loading. The multiaxial fatigue campaign comprised different normal stress to shear stress ratios and different nominal stress amplitudes. The sites of fatigue crack initiation and the angles of fatigue crack initiation were determined from the distributions of the first principal stress. Fatigue lives were predicted using an energy field intensity approach formalised in a linear-elastic framework combined with a local stress-strain model for notch plasticity analysis. The following conclusions can be drawn:

- The process of fatigue crack initiation was characterised by the nucleation and growth of two cracks in diametrically opposite sides of the hole. The increase of the shear stress level moved these locations to more interior points of the spherical surface, which was confirmed by both scanning electron microscopy and numerical simulation;
- The proposed criterion based on the maximum value of the first principal stress at the notch surface was capable to capture the sites of fatigue crack initiation for this geometric discontinuity when subjected to proportional bending-torsion loading. More than 80% of the predicted values exhibited errors lower than $\pm 5^o$;
- The angles of fatigue crack initiation were also successfully predicted by accounting for the first principal direction at the crack initiation sites. More than 75% of the predicted values exhibited errors lower than $\pm 10^o$. The existence of local stress raisers introduced by the drilling process at the geometric discontinuity may have introduced some scatter;
- The pseudo-elastic equivalent von Mises stress computed at the crack initiation site was able to correlate both the fatigue crack initiation life and total fatigue life with the multiaxial loading scenario. On the contrary, the nominal von Mises stress was not an adequate fatigue damage quantifier for the tested conditions;
- The crack initiation regions exhibited distinct features of cleavage fracture, such as river patterns, feather marks, facets, etc., suggesting a brittle nature of fracture, while the crack propagation regions exhibited fatigue striations with partial development and evidence of annihilation, which is sign of crack propagation in a dominant mixed-mode condition;
- The new concept of energy field intensity, implemented in a linear-elastic framework in conjunction with a local stress-strain approach (e.g. Glinka's rule or Neuber's rule) for notch plasticity analysis, was sufficiently accurate to assess the fatigue crack initiation life in notched geometries subjected to proportional bending-torsion loading;
- The fatigue crack initiation lives predicted with the proposed energy-based approaches correlated well with the experimental results. In both cases, all points were within scatter bands with factors of ± 2. Overall, the Neuber's approach was slightly less conservative than the Glinka's approach, but the differences were not significant.

Declaration of Competing Interest

The authors declare that they have no known competing financial interests or personal relationships that could have appeared to influence the work reported in this paper.

Acknowledgements

This research is sponsored by FEDER funds through the program COMPETE – Programa Operacional Factores de Competitividade – and by national funds through FCT – Fundação para a Ciência e a Tecnologia – under the project UIDB/00285/2020.

References

[1] Ashkenazi D. How aluminum changed the world: a metallurgical revolution through technological and cultural perspectives. Technol Forecast Soc Chang 2019; 143:101–13.
[2] Zhang X, Chen Y, Hu J. Recent advances in the development of aerospace materials. Prog Aerosp Sci 2018;97:22–34.
[3] Masoudi Nejad R, Berto F, Tohidi M, Jalayerian Darbandi A, Sina N. An investigation on fatigue behavior of AA2024 aluminum alloy sheets in fuselage lap joints. Eng Fail Anal 2021;126:105457.
[4] Moreira M. Failure analysis in aluminium turbocharger wheels. Eng Fail Anal 2016; 61:108–18.
[5] Liao D, Zhu S, Correia J, Jesus A, Calçada R. Computational framework for multiaxial fatigue life prediction of compressor discs considering notch effects. Eng Fract Mech 2018;202:423–35.
[6] Masoudi Nejad R, Berto F. Fatigue crack growth of a railway wheel steel and fatigue life prediction under spectrum loading conditions. Int J Fat 2022;157: 106722.
[7] Carpinteri A, Kurek M, Łagoda T, Vantadori S. Estimation of fatigue life under multiaxial loading by varying the critical plane orientation. Int J Fat 2017;100: 512–20.
[8] Gates N, Fatemi A. Multiaxial variable amplitude fatigue life analysis including notch effects. Int J Fat 2016;91:337–51.
[9] Berto F, Ayatollahi MR, Borsato T, Ferro P. Local strain energy density to predict size-dependent brittle fracture of cracked specimens under mixed mode loading. Theor Appl Fract Mech 2016;86:217–24.
[10] Carpinteri A, Fortese G, Ronchei C, Scorza D, Vantadori S. Spectral fatigue life estimation for non-proportional multiaxial random loading. Theor Appl Fract Mech 2016;83:67–72.
[11] Yang S, Sun J. Multiaxial fatigue life assessment of 304 austenitic stainless steel with a novel energy-based criterion. Int J Fat 2022;2022(159):106728.
[12] Susmel L, Atzori B, Meneghetti G, Taylor D. Notch and mean stress effect in fatigue as phenomena of elasto-plastic inherent multiaxiality. Eng Fract Mech 2011;78(8): 1628–43.
[13] Ferro P, Petrone N. Asymptotic thermal and residual stress distributions due to transient thermal loads. Fatigue Fract Eng Mater Struct 2009;32:936–48.
[14] Zhu SP, Liu Y, Liu Q, Yua ZY. Strain energy gradient-based LCF life prediction of turbine discs using critical distance concept. Int J Fat 2018;113:33–42.
[15] Marciniak Z, Rozumek D, Lesiuk G, Correia JAFO. Fatigue failure assessment of S355J2G1W structural steel under biaxial in- and out of phase loading regarding geometrical constraints of samples. Eng Fail Anal 2020;117:104785.
[16] Cruces AS, Mokhtarishirazabad M, Moreno B, Zanganeh M, Lopez-Crespo P. Study of the biaxial fatigue behaviour and overloads on S355 low carbon steel. Int J Fatigue 2020;134:105466.
[17] Benedetti M, Santus C, Raghavendra S, Lusuardi D, Zanini F, Carmignato S. Multiaxial plain and notch fatigue strength of thick-walled ductile cast iron EN-GJS-600-3: Combining multiaxial fatigue criteria, theory of critical distances, and defect sensitivity. Int J Fat 2022;156:106703.
[18] Costa JDM, Abreu LMP, Pinho ACM, Ferreira JAM. Fatigue behaviour of tubular AlMgSi welded specimens subjected to bending–torsion loading. Fatigue Fract Eng Mater Struct 2005;28(4):399–407.
[19] Macek W. Fractal analysis of the bending-torsion fatigue fracture of aluminium alloy. Eng Fail Anal 2019;99:97–107.
[20] Rozumek D, Faszynka S. Surface cracks growth in aluminum alloy AW-2017A-T4 under combined loadings. Eng Fract Mech 2020;226:106896.
[21] Susmel L, Petrone N. Multiaxial fatigue life estimations for 6082-T6 cylindrical specimens under in-phase and out-of-phase biaxial loadings. European Structural Integrity Society, vol. 31. Elsevier; 2003. p. 83–104.
[22] Singh A, Datta S, Chattopadhyay A, Riddick J, Hall A. Fatigue crack initiation and propagation behavior in Al – 7075 alloy under in-phase bending-torsion loading. Int J Fat 2019;126:346–56.
[23] Singh AK, Datta S, Chattopadhyay A, Phan N. Effects of overload mode-mixity on fatigue damage behavior and governing micromechanisms in AA7075 under biaxial fatigue loading. Int J Fat 2021;145:106141.
[24] Singh AK, Datta S, Chattopadhyay A, Phan N. Characterization of crack propagation behavior in Al-7075 under in-plane biaxial fatigue loading with shear overloads. Int J Fat 2020;134:105529.
[25] Kluger K, Łagoda T. New energy model for fatigue life determination under multiaxial loading with different mean values. Int J Fat 2014;66:229–45.
[26] Abreu LMP, Costa JD, Ferreira JAM. Fatigue behaviour of AlMgSi tubular specimens subjected to bending–torsion loading. Int J Fatigue 2009;31(8-9): 1327–36.
[27] Kluger K. Fatigue life estimation for 2017A–T4 and 6082–T6 aluminium alloys subjected to bending-torsion with mean stress. Int J Fat 2015;80:22–9.
[28] Karolczuk A, Kluger K, Palin-Luc T. Fatigue failure probability estimation of the 7075–T651 aluminum alloy under multiaxial loading based on the life-dependent material parameters concept. Int J Fat 2021;147:106174.
[29] Zhao B, Xie L, Wang L, Hu Z, Zhou S, Bai X. A new multiaxial fatigue life prediction model for aircraft aluminum alloy. Int J Fat 2021;143:105993.
[30] Liao D, Zhu S-P, Correia JAFO, De Jesus AMP, Berto F. Recent advances on notch effects in metal fatigue: A review. Fatigue Fract Eng Mater Struct 2020;43(4): 637–59.
[31] Peterson RE. Notch sensitivity. In: Sines G, Waisman JL, editors. Metal Fatigue. New York: McGraw Hill; 1958. p. 293–306.
[32] Liao D, Zhu SP. Energy field intensity approach for notch fatigue analysis. Int J Fat 2019;127:190–202.
[33] Neuber H. Theory of stress concentration for shear strained prismatical bodies with arbitrary non-linear stress-strain law. J Appl Mech 1961;28:544–50.
[34] Molski K, Glinka G. A method of elastic–plastic stress and strain calculation at a notch root. Mater Sci Eng 1981;50(1):93–100.
[35] Branco R, Costa JD, Borrego LP, Berto F, Razavi SMJ, Macek W. Comparison of different one-parameter damage laws and local stress-strain approaches in multiaxial fatigue life assessment of notched components. Int J Fat 2021;151: 106405.
[36] Branco R, Costa JD, Borrego LP, Wu SC, Long XY, Zhang FC. Effect of strain ratio on cyclic deformation behaviour of 7050–T6 aluminium alloy. Int J Fat 2019;129: 105234.
[37] Branco R, Costa JD, Borrego LP, Wu SC, Long XY, Antunes FV. Effect of tensile pre-strain on low-cycle fatigue behaviour of 7050–T6 aluminium alloy. Eng Fail Anal 2020;114:104592.
[38] Branco R, Costa JD, Berto F, Kotousov A, Antunes FV. Fatigue crack initiation behaviour of notched 34CrNiMo6 steel bars under proportional bending-torsion loading. Int J Fat 2020;130:105268.
[39] Luo P, Yao W, Susmel L, Li P. Prediction of fatigue damage region with the use of the notch critical plane approach for crack initiation and propagation. Int J Fatigue 2020;135:105533.
[40] Zerres P, Brüning J, Vormwald M. Fatigue crack growth behavior of fine-grained steel S460N under proportional and non-proportional loading. Eng Fract Mech 2010;77(11):1822–34.
[41] Shang DG. A new approach to the determination of fatigue crack initiation size. Int J Fatigue 1998;20:683–7.
[42] El Haddad MH, Topper TH, Smith KN. Prediction of non propagating cracks. Eng Fract Mech 1979;11(3):573–84.
[43] Antunes FV, Prates PA, Camas D, Sarrazin-Baudoux C, Gardin C. Numerical prediction of fatigue threshold of metallic materials in vacuum. Eng Fract Mech 2019;216:106491.
[44] Branco R, Costa JD, Antunes FV. Fatigue behaviour and life prediction of lateral notched round bars under bending–torsion loading. Eng Fract Mech 2014;119: 66–84.
[45] Handbook ASM. Fractography, vol.12 (ASM international Materials); 1987.
[46] Cina B, Kaatz T. A systematic study of the fractography of fatigue in high strength aluminium alloys. Fatigue Fract Eng Mater Struct 1979;2(1):85–95.
[47] Hao M-F, Zhu S-P, Liao D. New strain energy-based critical plane approach for multiaxial fatigue life prediction. J Strain Anal Eng Des 2019;54(5-6):310–9.
[48] Liu J, Ran Y, Xie L, Xue W. Multiaxial fatigue life prediction method of notched specimens considering stress gradient effect. Fatigue Fract Eng Mater Struct 2021; 44(5):1406–19.
[49] Lesiuk G, Szata M, Rozumek D, Marciniak Z, Correia J, De Jesus A. Energy response of S355 and 41Cr4 steel during fatigue crack growth process. J Strain Anal Eng 2018;53(8):663–75.
[50] Cicero S, García T, Álvarez JA, Klimpel A, Bannister A, Martín-Meizoso A. Fatigue behaviour and BS7608 fatigue classes of steels with thermally cut holes. J Constr Steel Res 2016;128:74–83.
[51] Branco R, Prates PA, Costa JD, Borrego LP, Berto F, Kotousov A, et al. Rapid assessment of multiaxial fatigue lifetime in notched components using an averaged strain energy density approach. Int J Fat 2019;124:89–98.
[52] Santus C, Taylor D, Benedetti M. Experimental determination and sensitivity analysis of the fatigue critical distance obtained with rounded V-notched specimens. Int J Fat 2018;113:113–25.
[53] Li DH, Shang DG, Xue L, Li LJ, Wang LW, Cui J. Notch stress-strain estimation method based on pseudo stress correction under multiaxial thermo-mechanical cyclic loading. Int J Solids Struct 2020;199:144–57.
[54] Vantadori S, Carpinteri A, Fortese G, Ronchei C, Scorza D, Zanichelli A. Fatigue lifetime evaluation of notched components: Implementation of the control volume concept in a strain-based LCF criterion. Theor Appl Fract Mech 2018;97:400–8.
[55] Ronchei C, Vantadori S. Notch fatigue life estimation of Ti-6Al-4V. Eng Fail Anal 2021;120:105098.
[56] Branco R, Prates PA, Costa JD, Berto F, Kotousov A. New methodology of fatigue life evaluation for multiaxially loaded notched components based on two uniaxial strain-controlled tests. Int J Fat 2018;111:308–20.